


Discovery of recombining plasma associated with the candidate supernova remnant G189.6+3.3 with Suzaku

Shigeo YAMAUCHI,^{1,*} Moe OYA,¹ Kumiko K. NOBUKAWA ,^{1,2} and Thomas G. PANNUTI³

¹Faculty of Science, Nara Women's University, Kita-uoyanishimachi, Nara, Nara 630-8506, Japan

²Department of Physics, Kindai University, 3-4-1 Kowakae, Higashi-Osaka, Osaka 577-8502, Japan

³Department of Physics, Earth Science and Space Systems Engineering, Morehead State University, 235 Martindale Drive, Morehead, KY 40351, USA

*E-mail: yamauchi@cc.nara-wu.ac.jp

Received 2019 December 6; Accepted 2020 July 6

Abstract

We present the results of an X-ray spectral analysis of the northeast region of the candidate supernova remnant G189.6+3.3 with Suzaku. K-shell lines from highly ionized Ne, Mg, Si, and S were detected in the spectrum for the first time. In addition, a radiative recombining continuum (RRC) from He-like Si was clearly seen near 2.5 keV. This detection of an RRC reveals for the first time that G189.6+3.3 possesses an X-ray-emitting recombining plasma (RP). The extracted X-ray spectrum in the 0.6–10.0 keV energy band is well fitted with a model consisting of a collisional ionization equilibrium plasma component (associated with the interstellar medium) and an RP component (associated with the ejecta). The spectral feature shows that G189.6+3.3 is most likely to be a middle-aged SNR with an RP.

Key words: ISM: individual objects (G189.6+3.3) — ISM: supernova remnants — X-rays: ISM

1 Introduction

Supernovae (SNe) release tremendous amounts of energy and are the main agents in the Universe for the synthesis of atoms of heavy elements. The supernova remnants (SNRs) help transfer the energy of SNe into the surrounding interstellar medium (ISM) and are the leading candidates for the acceleration of cosmic-ray particles to approximately the “knee” energy of the cosmic-ray spectrum. The expanding shock wave associated with SNRs sweeps up circumstellar matter and produces an X-ray-emitting plasma comprising both ISM and stellar ejecta. One quantity that describes the plasma is the electron temperature kT_e . This temperature, which corresponds to the temperature of the electrons of

the plasma, gradually increases over time through Coulomb collisions between the electrons and more energetic particles in the plasma. Furthermore, these energetic electrons ionize neutral atoms within the plasma. The temperature of these ionized atoms, denoted as the ionization temperature kT_i , is another quantity that describes the plasma, and typically kT_i follows kT_e . In general, the X-ray emitting plasmas associated with SNRs are not in a collisional ionization equilibrium (CIE) state where $kT_e = kT_i$ but instead in an ionizing plasma (IP) state where $kT_e > kT_i$. This is because the ionization-dominant phase of SNRs typically lasts $>10^4$ yr. Therefore, the X-ray spectra of most young and middle-aged SNRs are well-fitted with an IP model.

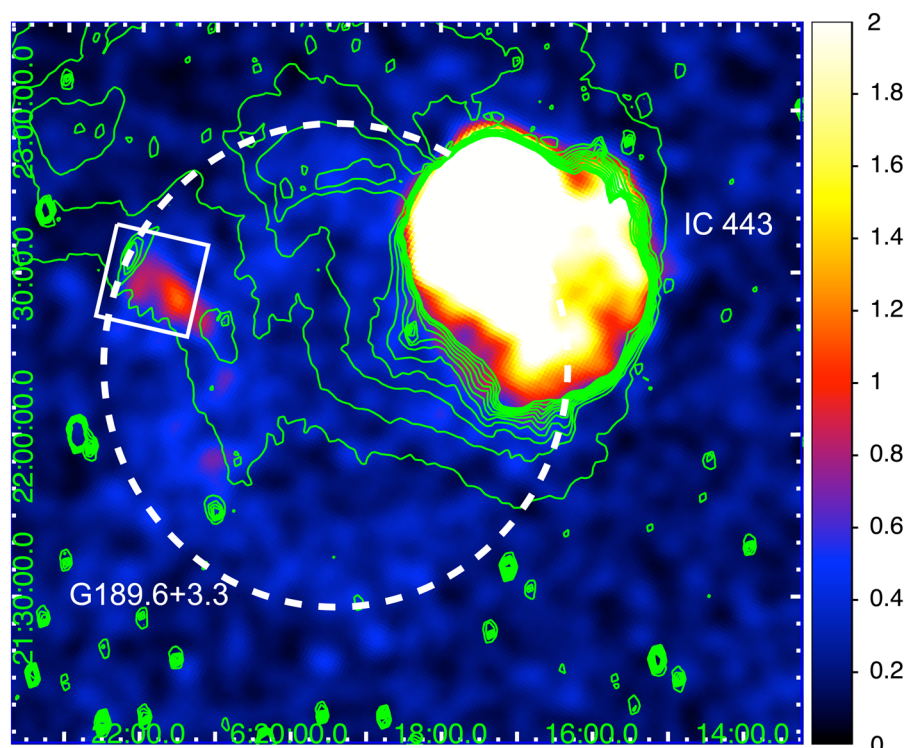


Fig. 1. X-ray (ROSAT, color) and radio band (1420 MHz, processed by the Canadian Galactic Plane Survey Consortium, green contour) images of G189.6+3.3 and IC 443 region, taken from the catalog of High Energy Observations of Galactic Supernova Remnants (Ferrand & Safi-Harb 2012).¹ Only the lower intensity levels are displayed. The color bar shows the intensity levels in arbitrary units. The coordinates are J2000.0. The white dashed line indicates an approximate shape of G189.6+3.3, while the white solid line shows the Suzaku XIS FOV. (Color online)

In the last decade, strong radiative recombination continua (RRCs) were discovered in the X-ray spectra of several Galactic SNRs, including IC 443 (Yamaguchi et al. 2009) and W49B (Ozawa et al. 2009). Since the RRC originates from radiative transitions where free electrons become bound to ions, a strong RRC is a sign of a recombining plasma (RP), which is characterized by $kT_e < kT_i$. Examples of Galactic SNRs that possess recombining plasmas—in addition to the SNRs mentioned above—are G359.1–0.5 (Ohnishi et al. 2011), W 28 (Sawada & Koyama 2012), W 44 (Uchida et al. 2012), and G346.6–0.2 (Yamauchi et al. 2013).

Since the formation of an RP is not predicted by a standard scenario of plasma evolution after the explosion described above, its formation must have been driven by special circumstances in the prior history of the SNR. Several scenarios that may explain the formation of the RP have been proposed in the literature. For example, in the conduction scenario, kT_e drops below kT_i by conductive cooling by a cold cloud (e.g., Kawasaki et al. 2002; Matsumura et al. 2017). Another scenario—known as the rarefaction scenario—proposes that adiabatic cooling occurs when the plasma breaks out from a dense medium into a much less dense medium (e.g., Masai 1994; Yamaguchi et al. 2018). Other proposed scenarios suggest

that kT_i increases by either photo-ionization by an external X-ray source (e.g., Nakashima et al. 2013; Ono et al. 2019) or by ionization due to low-energy cosmic rays (LECRs; e.g., Hirayama et al. 2019). The precise origin of RPs associated with SNRs remains uncertain, and realizing a clear understanding of their origin within the evolution of SNR plasmas is an outstanding unresolved issue.

The candidate SNR G189.6+3.3 was discovered by the ROSAT All-Sky Survey (Asaoka & Aschenbach 1994). The image of G189.6+3.3 revealed a ring-like X-ray morphology with a diameter of $\sim 1.5^\circ$. The center of this SNR is offset from the center of the nearby prominent SNR IC 443 by $\sim 0.7^\circ$ (see figure 1). The northeast region of G189.6+3.3 has the highest surface brightness in both the soft X-ray band (Asaoka & Aschenbach 1994) and the radio band, specifically at 327 MHz (Braun & Strom 1986). Analysis of the extracted X-ray spectrum of G189.6+3.3 revealed that the X-ray emission is mainly soft with a characteristic temperature of 0.14 keV. This result indicates that G189.6+3.3 is approximately 10^5 years old and is therefore a well-evolved SNR. Asaoka and Aschenbach (1994) argued that G189.6+3.3 lies in front of a molecular cloud that is itself known to lie in front of IC 443. Those authors

¹ (<http://snrcat.physics.umanitoba.ca/>).

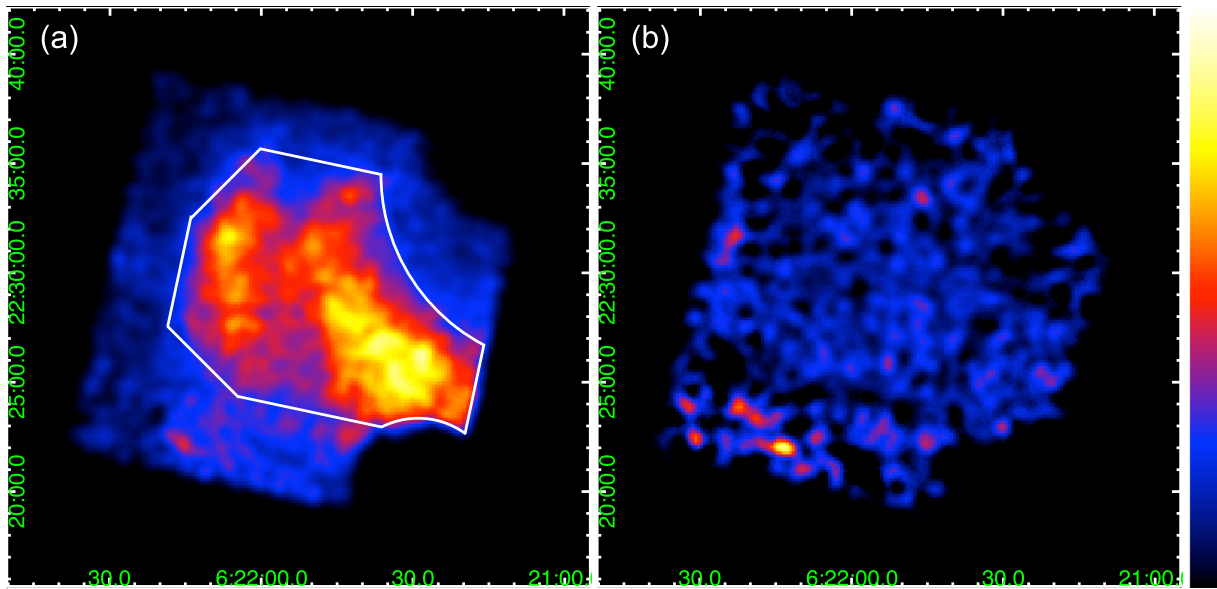


Fig. 2. XIS images of the northeast region of G189.6+3.3: (a) a soft X-ray band (0.6–3 keV) image and (b) a hard X-ray band (3–8 keV) image. NXB subtraction and vignetting correction were applied to both images. The coordinates are J2000.0. The color scale is linear (peak to bottom). The white solid line shows the region from which the X-ray spectrum is extracted. (Color online)

therefore estimated a distance to G189.6+3.3 of approximately 1.5 kpc.

After the analysis of the ROSAT observation of G189.6+3.3 by Asaoka and Aschenbach (1994), there has been no further detailed analysis in the literature of the X-ray properties of this SNR. Suzaku (Mitsuda et al. 2007) observed a northeast region (the brightest region) of G189.6+3.3. We analyzed the Suzaku archival data and discovered evidence for an RP associated with G189.6+3.3. In this paper, we report results of our spectral analysis. The quoted errors are at the 90% confidence level unless otherwise mentioned.

2 Observations and data reduction

The Suzaku observation of the northeast region of G189.6+3.3 was conducted on March 15–17 in 2015 (Obs. ID 509036010) with the X-ray Imaging Spectrometer (XIS; Koyama et al. 2007). The observed field is shown in figure 1. The XIS consisted of four sensors: XIS sensor-1 (XIS 1) is a back-side illuminated CCD (BI), while the other three XIS sensors (XIS 0, 2, and 3) are a front-side illuminated CCD (FI). Since XIS 2 ceased to function properly in 2006, observations were made with XIS 0, XIS 1 and XIS 3. A small fraction of the collecting area of XIS 0 was not used because of damage, possibly due to the impact of a micrometeorite on 2009 June 23. The XIS—which was operated in the normal clocking mode during the observation—employed the spaced-row charge injection (SCI) technique to rejuvenate its spectral resolution by filling the charge

traps with artificially injected electrons through CCD readouts. Details concerning the SCI technique are given in Nakajima et al. (2008) and Uchiyama et al. (2009).

Data reduction and analysis were made using HEASoft version 6.25. The XIS pulse-height data for each X-ray event were converted to pulse-invariant (PI) channels using the *xispi* software and the calibration database version 2018-10-10. We screened the data using the standard criteria. During the observations, count rates of the non-X-ray background (NXB) of XIS 1 were systematically higher than those of the NXB data generated by *xisnxbgen* (Tawa et al. 2008). Therefore, we utilized only the FI in the following analysis. The exposure times after applying the screening criteria are 66.1 ks for XIS 0 and 86.2 ks for XIS 3.

3 Analysis and results

3.1 Image

Figure 2 shows X-ray images in the “soft” (0.6–3.0 keV) and “hard” (3.0–8.0 keV) energy bands of G189.6+3.3 using the XIS. Consistent with the ROSAT image and the analysis of Asaoka and Aschenbach (1994), the soft X-ray band image clearly shows the presence of diffuse X-ray emission. We compared the soft X-ray image with radio maps of this SNR (Braun & Strom 1986; Leahy 2004) and found that the X-ray emission in this band is located just inside of the radio shell (see figure 1). On the other hand, the hard X-ray band image shows no significant emission and we therefore conclude that the X-ray spectrum of G189.6+3.3 is primarily soft.

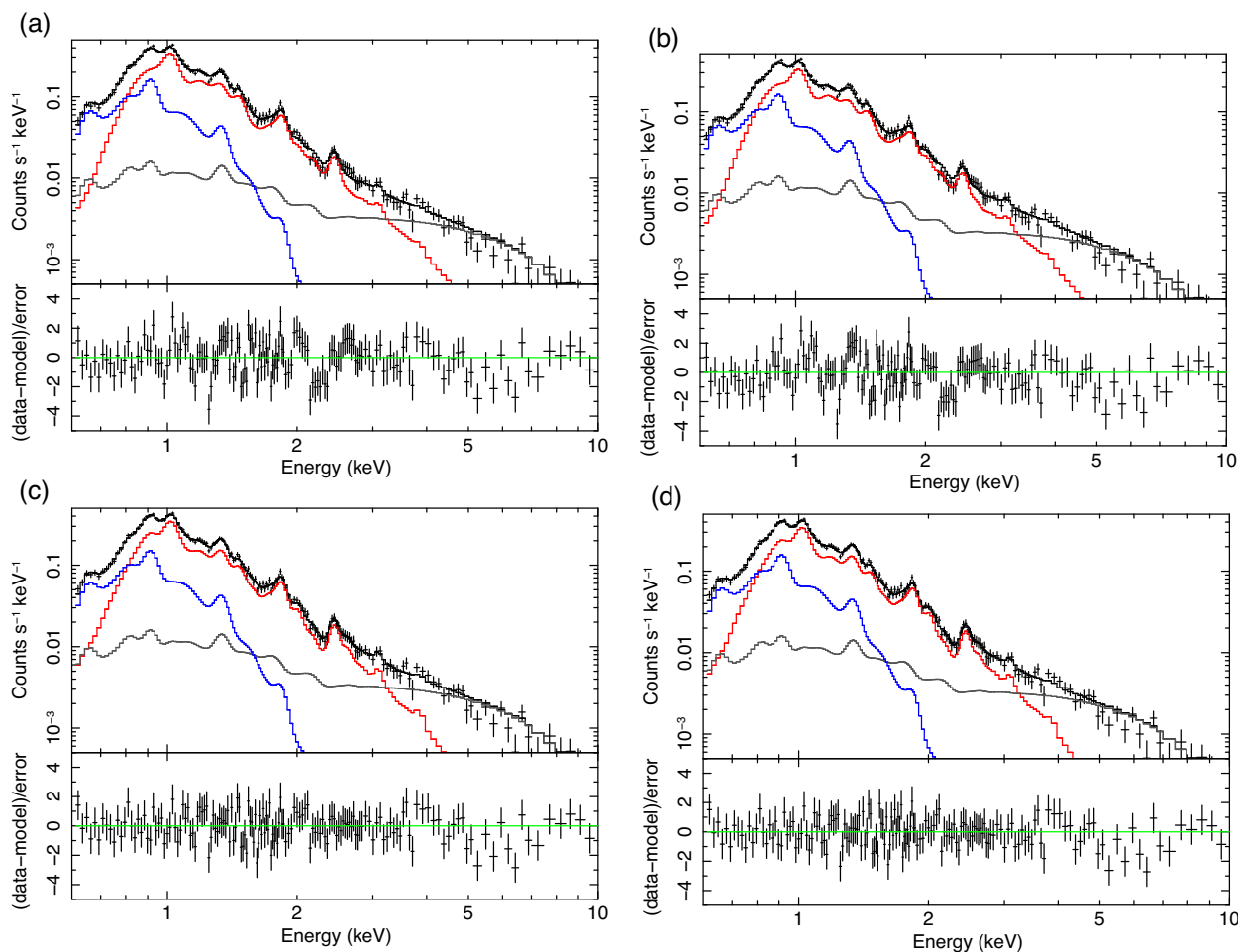


Fig. 3. XIS spectrum of the northeast region (upper panel) and residuals from the best-fitting model (lower panel), (a) model A, (b) model B, (c) model C, and (d) model D. Errors of the data points are at the 1σ level. The blue, red, and gray solid lines show emission from ISM, ejecta, and the sky background (MWH+LHB+CXB) components, respectively. (Color online)

3.2 Spectrum

Based on the work of Masui et al. (2009), we modeled the sky background spectrum, which consists of the Milky Way Halo (MWH), Local Hot Bubble (LHB), and Cosmic X-ray Background (CXB). The values of the parameters of the MWH and LHB were assumed to be the same as the values used in Hirayama et al. (2019), while those of the CXB were fixed to the values in Kushino et al. (2002). It is known that another diffuse source of X-ray emission known as the Galactic diffuse X-ray emission (GDXE) (Koyama 2018) exists along the Galactic plane. However, since G189.6+3.3 is located at the anti-center region with the Galactic latitude of $b = 3.3^\circ$, where the contamination of the GDXE is small (Uchiyama et al. 2013; Yamauchi et al. 2016), we ignored this component of diffuse emission in our spectral analysis.

The source spectrum of G189.6+3.3 was extracted from the region indicated in figure 2. The NXB was estimated using `xisnxbgen` (Tawa et al. 2008) and was

subtracted from the source spectrum. Figure 3 shows the NXB-subtracted spectrum of G189.6+3.3: the contributions of the sky background from the different components (MWH + LHB + CXB) are indicated with a solid gray line.

To fit the extracted source spectrum, we first applied a CIE model (corresponding to the `vapex` model in XSPEC) combined with a low-energy absorption model. The cross-section of the photoelectric absorption and the abundance tables were taken from Balucinska-Church and McCammon (1992) and Anders and Grevesse (1989), respectively. In the spectral fitting, we corrected the energy scale using a linear function. Residuals were seen in the spectrum in the 0.6–1.0 keV band: to address these, we added another CIE model with solar abundances to represent emission from a shocked ISM component. We denote this first combined model for fitting as Model A and note that Model A failed to provide a statistically-acceptable fit to the source spectrum ($\chi^2/\text{d.o.f.} = 224.6/151 = 1.49$). We also found systematic residuals around 2.5 keV: the

Table 1. Best-fitting parameters of CIE (Model A), single-RP (Model B), two-temperature RP (Model C), and multi- kT_0 RP (Model D).

		Values							
Component	Parameter	Model A	Model B		Model C		Model D		
Absorption	N_{H}^*	6.0 ± 0.4	5.9 ± 0.4		5.9 ± 0.4		6.2 ± 0.7		
ISM (CIE)	kT_{e}^\dagger	0.18 ± 0.01	0.18 ± 0.01		0.18 ± 0.02		0.18 ± 0.02		
	Normalization ‡	0.038 ± 0.010	0.035 ± 0.009		0.031 ± 0.010		0.038 ± 0.014		
Ejecta (RP1)	kT_{e}^\dagger	0.79 ± 0.04	0.78 ± 0.05		0.45 ± 0.04		0.46 ± 0.07		
	Normalization ‡	0.0030 ± 0.0003	0.0028 ± 0.003		0.0030 ± 0.004		0.0032 ± 0.0011		
	$n_{\text{e}} t^\S$	—	11^{+7}_{-3}		6.0 ± 0.7		$1.8^{+4.5}_{-1.2}$		
		Ab^\parallel	kT_0^\dagger	Ab^\parallel	kT_0^\dagger	Ab^\parallel	kT_0^\dagger	Ab^\parallel	
	H=He=C=N=O	1 (fixed)	(link to Ne)	1 (fixed)	(link to Ne)	1 (fixed)	(link to Ne)	1 (fixed)	
	Ne	6.0 ± 1.0	3.0 (fixed)	6.7 ± 1.1	$3.0^{+2.2}_{-0.9}$	6.1 ± 1.9	$0.50^{+0.71}_{-0.08}$	$5.1^{+3.1}_{-2.2}$	
	Mg	1.2 ± 0.2	(link to Ne)	1.3 ± 0.3	(link to Ne)	3.0 ± 0.6	$0.79 (>0.69)$	$2.8^{+1.2}_{-0.8}$	
	Si	0.8 ± 0.2	(link to Ne)	0.9 ± 0.2	(link to Ne)	3.2 ± 0.7	$1.2 (>1.0)$	3.0 ± 1.0	
	S=Ar=Ca	1.0 ± 0.3	(link to Ne)	1.1 ± 0.3	—	0 (fixed)	—	0 (fixed)	
	Fe=Ni	1 (fixed)	(link to Ne)	1 (fixed)	—	0 (fixed)	—	0 (fixed)	
	Ejecta (RP2)	kT_{e}^\dagger	—	—		0.73 ± 0.05		0.67 ± 0.13	
		Normalization ‡	—	—		(link to RP1)		(link to RP1)	
$n_{\text{e}} t^\S$		—	—		(link to RP1)		(link to RP1)		
H-Si		—	—	—	—	0 (fixed)	—	0 (fixed)	
S=Ar=Ca		—	—	—	(link to Ne)	1.8 ± 0.5	$1.5^{+2.2}_{-0.3}$	1.9 ± 0.6	
Fe=Ni		—	—	—	(link to Ne)	1 (fixed)	$1.1^{+3.4}_{-0.3}$	1 (fixed)	
$\chi^2/\text{d.o.f.}$		$224.6/151 = 1.49$	$235.4/150 = 1.57$		$151.0/148 = 1.02$		$146.1/144 = 1.01$		

*The unit is $\times 10^{21} \text{ cm}^{-2}$.

† Units are keV. kT_e is an electron temperature at the present time and kT_0 is an initial ionization temperature at $n_e t = 0$.

‡ Defined as $10^{-14} \times \int n_{\text{H}} n_e dV / (4\pi D^2)$ (cm^{-5}), where D is the distance (cm), n_{H} is the hydrogen density (cm^{-3}), n_e is the electron density (cm^{-3}), and V is the volume (cm^3).

§ Recombination time scale, where n_e is the electron density (cm^{-3}) and t is the elapsed time (s). The unit is $\times 10^{11} \text{ cm}^{-3} \text{ s}$.

$^\parallel$ Relative to the solar values in Anders and Grevesse (1989).

presence of these residuals—combined with positive residuals at the energy of the Si Ly α line—suggested the presence of an RRC from He-like Si (see figure 3a).

The implied presence of an RRC motivated us to apply an RP model (corresponding to the `vrnei` model in XSPEC) for the ejecta component of the observed X-ray emission. Similar to our results with the CIE model, we again found residuals in the 0.6–1.0 keV energy range, and added the shocked ISM component. We denote this combined CIE+RP model as Model B and note that this combined model also failed to yield a statistically-acceptable fit to the spectrum ($\chi^2/\text{d.o.f.} = 235.4/150 = 1.57$). Inspection of the fit obtained with this model revealed that the Mg He α line and the RRC structure remain in the fit residuals (see figure 3b). These suggest that kT_e of the lighter elements differs from kT_e of the heavier elements. As our next step, we applied a two-electron temperature RP model (denoted as Model C). Specifically, the first RP component (denoted as RP1) consists of the elements H through Si, while the second component (denoted as RP2) consists of S through Ni. While the electron temperatures of RP1 and RP2 were varied as free parameters independent of each other, other

parameters, specifically the recombination timescale, the initial temperature kT_0 , and the normalizations, were tied together. We found at last that Model C gave an acceptable fit to the source spectrum with $\chi^2/\text{d.o.f.} = 151.0/148 = 1.02$ (see table 1 and figure 3c).

In the case of Model C, the plasma is assumed to have the same kT_i for all the elements (which is consistent with CIE) at the epoch where the plasma made a transition into an RP. However, we note that attaining CIE is not an inevitable condition for plasmas associated with SNRs. For example, in analyzing Suzaku data for W 28, Sawada and Koyama (2012) examined the time evolution of RPs with the same kT_0 for all elements (again consistent with CIE) and a different kT_0 for each element, and showed that the spectrum could be fitted adequately in both cases. Furthermore, Hirayama et al. (2019) applied a multi- kT_0 RP model, where each element has its own value for kT_0 , to the high-quality spectrum of IC 443, and showed the spectrum is represented by the model. We followed the examples by these authors and attempted to fit the source spectrum of G189.6+3.3 with a multi- kT_0 RP model, which we denote as Model D. We obtained a statistically-acceptable fit with

this model as well ($\chi^2/\text{d.o.f.} = 146.1/144 = 1.01$). The improvement from the Model C fit is not statistically significant. The best-fitting parameters of this model are listed in table 1 and the model itself is plotted in figure 3d.

4 Discussion

Our work presented here confirmed that G189.6+3.3 features an extended X-ray emission that is located just inside a shell-like feature observed in the radio band. The results of our spectral analysis revealed that the X-ray emission from stellar ejecta associated with this SNR is best-represented by an optically-thin thermal plasma model with an electron temperature $kT_e \sim 0.4\text{--}0.7\text{ keV}$. In addition, an RRC from He-like Si is clearly detected around 2.5 keV: the presence of this RRC is evidence that the X-ray emitting plasma associated with G189.6+3.3 is an RP. The spectral features of this SNR resemble other middle-aged SNRs that also possess an RP (e.g., Yamaguchi et al. 2009; Ohnishi et al. 2011; Sawada & Koyama 2012; Uchida et al. 2012; Yamauchi et al. 2013). Therefore, G189.6+3.3 is also most likely to be a middle-aged SNR with an RP.

We obtained statistically-acceptable fits to the extracted X-ray spectra of G189.6+3.3 with Model C (a two-temperature RP model) and Model D (a multi- kT_0 RP model). In the case of the fit with Model C, the plasma is assumed to be in the CIE state at the epoch of transitioning into an RP. Note that the fitted initial temperature of the plasma with Model C is $\sim 3\text{ keV}$. A CIE plasma with this temperature is not typically seen in SNRs evolving in relatively low-density environments, but in the case of a supernova explosion that occurs in a high-density environment, a high temperature CIE plasma may be produced (e.g., Katsuda et al. 2016). In contrast, Model D represents an RP which is not initially in CIE. To explore this result further, we simulated IP spectra assuming various values of ionization timescales and kT_e , and fitted these spectra with a multi- kT_i model which has a different value for kT_i for each element. With this approach, we found that an IP spectrum with $kT_e \sim 2\text{ keV}$ and an ionization timescale of $\sim 2 \times 10^{11}\text{ cm}^{-3}\text{ s}$ is approximated by the multi- kT_i model in which kT_e is $\sim 2\text{ keV}$ and kT_i of each element is consistent with kT_0 of Model D. This result indicates that the initial condition described by the fitted parameters of Model D can approximate the non-equilibrium ionization state. Furthermore, the kT_0 values of Model D appear to increase with increasing atomic number over the range of elements from Ne to Ca. This result parallels those of the different kT_0 case attained by an IP as shown by Sawada and Koyama (2012). Therefore, an acceptable fit to the spectra using Model D implies that a scenario where the plasma transitions from an IP to an RP is possible. We note that

Model D assumes the ion population of a CIE plasma with kT_0 for each element, which is actually different from that of a real IP. To investigate this scenario, a plasma model taking into account the evolution from an IP at the initial epoch to an RP is needed.

As described previously, different scenarios to produce an RP, such as the thermal conduction scenario, the adiabatic expansion scenario, the scenario of photo-ionization by an external source and the scenario where ionization is accomplished by LECRs, have been presented in the literature. As applied to G189.6+3.3, we rule out the scenario of photo-ionization by an external source because no such bright sources have been found near this SNR so far. The remaining three scenarios cannot be ruled out at this time: both the thermal conduction and adiabatic expansion scenarios suggest that kT_e dropped significantly and therefore the plasma transitioned to an RP from either an IP or a state of CIE. To investigate either of these scenarios further, it is crucial to determine if the ISM that surrounds G189.6+3.3 is particularly dense or not. Regarding the scenario where ionization is accomplished by LECRs, it is important to note that the prominent X-ray emission from this SNR is located near the shell-like structure detected in the radio band (see figure 1). This result suggests that LECRs accelerated at the shell may be ionizing atoms and establishing the condition where $kT_e < kT_i$. For this scenario, however, more evidence is needed to indicate that particle acceleration is indeed occurring at this location. Since information about the physical conditions of the ISM surrounding G189.6+3.3 is limited, at this point we cannot further distinguish between any of these three scenarios for the origin of the RP.

The parameters of the best fits with Model C and Model D indicate that ions of lighter elements are described with lower electron temperatures. A similar relation between the atomic numbers of elements and their temperatures was found in an X-ray study of the Galactic SNR G272.2–3.2 (Kamitsukasa et al. 2016). This result may indicate that the plasma associated with G189.6+3.3 has a stratified structure with lighter elements located in outer layers of the plasma. In such a situation, the outer layers of the plasma would cool as the SNR expands.

Assuming the distance to be 1.5 kpc and the light-of-sight length of the thin thermal plasma to be 4.4 pc (corresponding to an angular extent of $10'$), we calculated several physical parameters of the X-ray emitting plasma associated with this SNR. Adopting a filling factor of 1, the volume of the plasma of $\sim 3 \times 10^{57}\text{ cm}^{-3}$ ($= 12' \times 10' \times 10'$), and $n_e = 1.2n_H$, where n_e and n_H are the electron and hydrogen densities, respectively, and applying the best-fitting parameters, we obtained values for the mean n_H , the gas mass, and the thermal energy of the ISM component of $\sim 0.5\text{ cm}^{-3}$,

$\sim 2 M_{\odot}$, and $\sim 1.5 \times 10^{48}$ erg, respectively. Similarly, for the mean n_{H} , gas mass, and thermal energy of the ejecta component, we derived values of $\sim 0.15 \text{ cm}^{-3}$, $\sim 0.5 M_{\odot}$, and $\sim 10^{48}$ erg, respectively. These calculated values for the mass and the thermal energy of the X-ray-emitting plasma associated with G189.6+3.3 indicate that the plasma only comprises a small portion of the total mass and total thermal energy of the whole SNR, when compared to other Galactic SNRs.

While our work has revealed the presence of an RP associated with G189.6+3.3, many properties of this intriguing SNR remain unknown. We strongly encourage new multi-wavelength observations of this source to probe its properties in more detail.

Acknowledgments

We would like to express our thanks to all of the Suzaku team. The authors wish to thank the referee for constructive comments that improved the manuscript. This work was supported by the Japan Society for the Promotion of Science (JSPS) KAKENHI Grant Numbers JP16J00548 (KKN).

References

- Anders, E., & Grevesse, N. 1989, *Geochim. Cosmochim. Acta*, 53, 197
- Asaoka, I., & Aschenbach, B. 1994, *A&A*, 274, 573
- Balucinska-Church, M., & McCammon, D. 1992, *ApJ*, 400, 699
- Braun, R., & Strom, R. G. 1986, *A&A*, 164, 193
- Ferrand, G., & Safi-Harb, S. 2012, *Adv. Space Res.*, 49, 1313
- Hirayama, A., Yamauchi, S., Nobukawa, K. K., Nobukawa, M., & Koyama, K. 2019, *PASJ*, 71, 37
- Kamitsukasa, F., Koyama, K., Nakajima, H., Hayashida, K., Mori, K., Katsuda, S., Uchida, H., & Tsunemi, H. 2016, *PASJ*, 68, S7
- Katsuda, S., et al. 2016, *ApJ*, 832, 194
- Kawasaki, M. T., Ozaki, M., Nagase, F., Masai, K., Ishida, M., & Petre, R. 2002, *ApJ*, 572, 897
- Koyama, K. 2018, *PASJ*, 70, R1
- Koyama, K., et al. 2007, *PASJ*, 59, S23
- Kushino, A., Ishisaki, Y., Morita, U., Yamasaki, N. Y., Ishida, M., Ohashi, T., & Ueda, Y. 2002, *PASJ*, 54, 327
- Leahy, D.A. 2004, *AJ*, 127, 2277
- Masai, K. 1994, *ApJ*, 437, 770
- Masui, K., Mitsuda, K., Yamasaki, N. Y., Takei, Y., Kimura, S., Yoshino, T., & McCammon, D. 2009, *PASJ*, 61, S115
- Matsumura, H., Tanaka, T., Uchida, H., Okon, H., & Tsuru, T. G. 2017, *ApJ*, 851, 73
- Mitsuda, K., et al. 2007, *PASJ*, 59, S1
- Nakajima, H., et al. 2008, *PASJ*, 60, S1
- Nakashima, S., Nobukawa, M., Uchida, H., Tanaka, T., Tsuru, T. G., Koyama, K., Murakami, H., & Uchiyama, H. 2013, *ApJ*, 773, 20
- Ohnishi, T., Koyama, K., Tsuru, T. G., Masai, K., Yamaguchi, H., & Ozawa, M. 2011, *PASJ*, 63, 527
- Ono, A., Uchiyama, H., Yamauchi, S., Nobukawa, M., Nobukawa, K. K., & Koyama, K. 2019, *PASJ*, 71, 52
- Ozawa, M., Koyama, K., Yamaguchi, H., Masai, K., & Tamagawa, T. 2009, *ApJ*, 706, L71
- Sawada, M., & Koyama, K. 2012, *PASJ*, 64, 81
- Tawa, N., et al. 2008, *PASJ*, 60, S11
- Uchida, H., et al. 2012, *PASJ*, 64, 141
- Uchiyama, H., et al. 2009, *PASJ*, 61, S9
- Uchiyama, H., Nobukawa, M., Tsuru, T. G., & Koyama, K. 2013, *PASJ*, 65, 19
- Yamaguchi, H., et al. 2018, *ApJ*, 868, L35
- Yamaguchi, H., Ozawa, M., Koyama, K., Masai, K., Hiraga, J. S., Ozaki, M., & Yonetoku, D. 2009, *ApJ*, 705, L6
- Yamauchi, S., Nobukawa, K. K., Nobukawa, M., Uchiyama, H., & Koyama, K. 2016, *PASJ*, 68, 59
- Yamauchi, S., Nobukawa, M., Koyama, K., & Yonemori, M. 2013, *PASJ*, 65, 6